Lawrence Berkeley National Laboratory

Title

Polaris-LAMP: Multi-Modal 3-D Image Reconstruction With a Commercial Gamma-Ray Imager

Permalink

https://escholarship.org/uc/item/45r822p9

Journal

IEEE Transactions on Nuclear Science, 68(10)

ISSN

0018-9499

Authors

Hecla, J
Knecht, K
Gunter, D
et al.

Publication Date

2021-10-01

DOI

10.1109/tns.2021.3110162

Peer reviewed

Polaris-LAMP: Multi-modal 3D Image Reconstruction with a Commercial Gamma-ray Imager

J. Hecla, K. Knecht, D. Gunter, A. Haefner, D. Hellfeld, T. H. Y. Joshi, A. Moran, V. Negut, R. Pavlovsky, K. Vetter

Abstract—The Polaris-LAMP multi-modal 3D gamma-ray imager is a radiation mapping and imaging platform which uses a commercial-off-the-shelf detector integrated with a contextual sensor localization and mapping platform. The integration of these systems enables a free-moving radiation imaging capability with proximity mapping, coded aperture, and Compton imaging modalities, which can create 3D reconstruction of photon sources from tens of keV to several MeV. Gamma-ray events are recorded using a segmented cadmium zinc telluride detector (Polaris-H Quad by H3D inc.), while scene data is derived from a contextual sensor and computation package developed by Lawrence Berkeley National Laboratory which includes GPS, laser ranging and inertial measurement sensors. An onboard computer uses these inputs to create rapidly-updating pose (10 Hz) and 3D scene estimates using a simultaneous localization and mapping algorithm. The precise gamma-ray event location and timing resolution of the Polaris CZT sensor enables Compton imaging above several hundred keV, while photon sources at lower images are localized using coded aperture imaging techniques. The multi-modal imaging concept enables imaging of diverse radiation sources spanning from the 59 keV emission of ^{241}Am to the 1.1 and 1.3 MeV lines of ^{60}Co. This work focuses on the description of the the operational principles of the detector system and demonstrating the 3D imaging performance in a variety of source detection and mapping scenarios. As a proof of concept, we demonstrate mapping complex environments, including both point source and distributed-source environments using proximity, coded aperture, and Compton imaging modalities. Further, we show the successful use of the system to perform measurements in high-background environments through analysis of arrays of uranium hexafluoride cylinders at the Paducah UF6 project site.

Index Terms—Compton imaging, Coded aperture imagers, Scene data fusion, 3D gamma-ray imaging

J. Hecla, K. Knecht, and K. Vetter are with the Nuclear Engineering Department at the University of California, Berkeley, Berkeley, CA 94720 USA (e-mail: jake_hecla@berkeley.edu).

D. Hellfeld, T. H. Y. Joshi, A. Moran, V. Negut, R. Pavlovsky, and K. Vetter are with the Applied Nuclear Physics (ANP) Program at Lawrence Berkeley National Laboratory (LBNL), Berkeley, CA 94720 USA (e-mail: thjoshi@lbl.gov).

A. Haefner was with the ANP Program at LBNL during this work and is now with GammaReality Inc., Richmond, CA 94804 USA.

D. Gunter is with Gunter Physics, Inc. at 6221 Trinity Dr., Lisle, IL 60532 USA

I. INTRODUCTION

THE localization and mapping of radiation sources in 3D is an emerging technique which offers significant speed and precision advantages over traditional source-search and dose-rate mapping methodologies [1]. This process is enabled by the supplementation of radiation interaction data with contextual information provided by LiDAR (light detection and ranging) and/or a camera, along with position information provided by GPS and/or an inertial measurement unit. The integration of contextual and position information with radiation interaction data is referred to as scene data fusion (SDF) [2]. SDF enables free-moving mapping, which breaks distance symmetries associated with static 2D sensing by sampling throughout 3D space. This method therefore offers a significant sensitivity and localization capability unavailable with traditional methods, as demonstrated by a variety of prior SDF systems [3], [4].

Non-SDF source search methods typically involve handheld radiation detection systems or imaging detectors. In the former method, sources are located using the operator's observation of the detector response as they move. Some users may employ collimators or shields in an attempt to impose modulation on the signal, which may enable more rapid location. These methods involve personnel dose, and are limited to the regions the operators can access.

Imaging systems can reduce the personnel dose associated with a measurement, as they are typically operated in a long-dwell, point-and-stare mode. Dwell times can range from minutes to hours, and offer a means of locating a source in angular space [5]. However, while these images can provide valuable context, the time associated with taking a single image and the 2D measurement modality limits this method to scenarios in which survey rates are low [6].

The Polaris-LAMP system integrates contextual sensors that allow mapping and localization of radiation sources in 3D space. The detector can be deployed similarly to a handheld survey meter, yet creates a 3D model of the surroundings with integrated radiation information derived from proximity mapping, coded-aperture, and Compton radiation imaging modalities, allowing imaging across a wide variety of sources. It is therefore faster than both hand-survey and 2D imaging methods, while providing a vastly improved localization capability. Furthermore, the data product consisting of a 3D map alongside list-mode interaction information allows post-processing and detailed retrospective analysis of scenes in a manner unavailable with other systems.

The detector system introduced here consists of a commercial off-the-shelf (COTS) radiation sensor – the Polaris-H

segmented cadmium zinc telluride (CZT) detector developed by H3D [7] – which provides event data (energy, timing, location) to a contextual sensor package developed by Lawrence Berkeley National Laboratory to generate 3D reconstructions [8].

In comparison to custom detector solutions, the Polaris system possesses a high level of technical maturity, and offers a 2D imaging capability [9]. The addition of the LAMP contextual sensor and scene data fusion package offers a means of using the detailed interaction data from Polaris to create detailed 3D models of the radiation environment around the detector. These 3D reconstructions can be performed using constraints based on LiDAR or camera-generated point clouds, and may be done in real time (delays of seconds) or in post-processing.

II. METHODS

A. Detector Module

The Polaris-H CZT detector module is a COTS system for radiation sensing and imaging produced by H3D Technologies (Ann Arbor, Michigan). The detector system (labeled in blue in Fig. 1) consists of four clustered $20{\times}20{\times}10$ mm^3 CZT crystals packaged with proprietary H3D ASICs for event processing. The raw-list mode data (energy, X-Y-Z position, and time for each event) acquired with the TCP/IP interface of the H3D detector is processed with our own analysis code. X-Y event localization is performed using segmented anodes ($12{\times}12$ per crystal) for a resolution of 0.5 mm due to sub-pixel binning [10]. The cathode-anode ratio or drift time is used for depth sensing [11], yielding approximately 1 mm depth resolution based on measurements taken using a collimated 662 keV source. To enable coded-aperture imaging, the detector uses a 1.5 mm thick rank-19 modified uniformly redundant array (MURA) mask [12] made of a machinable 97% tungsten alloy. This mask has a 50 % open fraction, and behaves as a binary mask with minimal transmission approximately 100 keV incident photon energy. The theoretical limit of the coded aperture mask resolution is 2.9 degrees FWHM using the formula given by Fenimore [13].

Pursuant to our testing, the detector has spectral resolution of approximately 1% FWHM at 662 keV [7] and 4.5% at 59.5 keV for all events. The effective energy range of the detector is approximately 40 keV to 2 MeV, the minimum of which is set by the device noise floor. Event rates are limited to approximately 27 kcps, though significant event arrival time anomalies are noted above 10 kcps (rates calculated assuming single interactions with no cuts). The photopeak efficiency of the detector is approximately 16% at 59.9 keV and 8% at 662keV. [7]. For detailed description of detector performance see [7] and [9].

B. Scene Data Fusion

SDF is the process by which radiation data and information on system surroundings are combined to create outputs which contextualize the detected radiation signatures [2]. This can be presented as a 2D or 3D map or image depicting the location and intensity of radiation sources.

SDF is possible with Polaris-LAMP due to system location and surroundings being returned from the LAMP module (labeled in purple in Fig. 1), which combines an onboard computer, LiDAR unit, visual camera, inertial measurement unit (IMU) and a GPS module to perform simultaneous localization and mapping (SLAM). SLAM algorithms [14] continuously update a map of the detector's surroundings and estimate the position and orientation of the detector within a scene at any point in time, referred to as the 'pose'. The SLAM solution provides the information necessary to perform 3D reconstructions [8]. The LAMP module uses a modified version of Google's Cartographer algorithm [15], and with current hardware, offers a pose uncertainty of 5–25 cm for local SLAM (e.g., over small areas). While SLAM is possible using a wide variety of sensors, the combination of LiDAR and an IMU is the most common and versatile sensor choice, and is used throughout this paper. LiDAR returns can be gathered and processed in real time, and most modules provide a 360-degree view of the surroundings, offering an ideal input for SLAM.

The contextual "scene" data is used to constrain the reconstruction to intersections of radiation backprojections with surfaces present in the scene, since we can assume that the radiation is being emitted from a physical object. The LiDAR collects laser scan data and the LAMP package processes the laser scans to build point clouds, which describe the objects in the scene as points in the 3D imaging space. The imaging space is divided into a voxelized grid, and occupancy of each voxel is determined. A voxel is considered to be occupied if the number of point cloud points which reside in it is greater than some cutoff value. These constraints allow the problem to be computationally tractable and help create a data product that reflects both the sensed environment and the computed gamma emitter distribution.

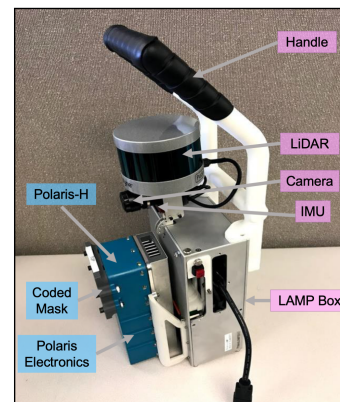Fig. 1. Image of the Polaris-LAMP detector. Note LiDAR module on top, and RGB camera below it. The coded aperture mask is contained in the grey plastic case mounted to the front of the Polaris module.

C. Imaging Modalities

The Polaris-LAMP system offers proximity mapping, coded aperture imaging, and Compton imaging modalities in a single package. In combination, these imaging modalities provide a

powerful ability to localize and map sources across a wide range of energy and source strengths.

1) Proximity reconstruction: Proximity mapping is a form of radiation mapping based on attenuation imposed by source-detector distance alone. In this modality, a detector is modeled as a point detector with a uniform angular response. The artifacts from a non-symmetric detector being modeled as a point detector are assumed to be negligible in the far-field. All signal modulation is ascribed to detector motion within a scene, and reconstruction is typically performed using iterative methods such as MLEM [16] using a scene constraint such as a LiDAR cloud [17] or Point Source Likelihood (PSL) and Additive Point Source Localization (APSL) [18] [19]. This method, while compuationally simple, offers low resolution mapping due to the lack of angular modulation, and is best suited for rapid and highly approximate mapping of contaminated areas.

The rate of events detected by a single-pixel system at position $\vec{x}$ can be described using an approximation for a finite time step (Δt) and voxels with activity Λ_s located at positions x_s:

$$R = \sum_{s=1}^{N_{vox}} \frac{\eta \Lambda_s \xi_s \Delta t}{4\pi \|\vec{x}_s - \vec{x}\|^2} + b\Delta(t), \quad (1)$$

where ξ_s is an attenuation term to represent the transmission of source photons from $\vec{x_s}$ to $\vec{x}$, η is detector efficiency and b is a constant background rate. In this work, we assume $\xi_s = 1$ and $b = 0$.

2) Compton imaging: Compton imaging offers a means of imaging sources with characteristic photon energies above a few hundred keV. This imaging modality relies on multiple interaction events within the detector volume. It is possible to consider events comprised of multiple Compton scatters which terminate in a photoelectric absorption, but in this analysis we consider only double interaction events, assuming one Compton scatter and one photoelectric absorption.

2D Compton imaging requires the 3D positions of the first two interactions associated with one gamma-ray event, which form the symmetry axis of a Compton cone. It also requires the energy of the incident gamma-ray and the energy deposited in the first interaction, which define the opening angle of the Compton cone through the following equation:

$$\cos\theta = 1 + m_e c^2 \left(\frac{1}{E_\gamma} - \frac{1}{E'_\gamma} \right), \quad (2)$$

in which:
- θ is the Compton cone opening angle
- m_e is rest mass of an electron
- c is the speed of light
- E_γ is incident gamma-ray energy
- E'_γ is outgoing gamma-ray energy

The incident gamma-ray energy is assumed to be the sum energy of the interactions that comprise an event. Spectroscopic imaging uses the events whose incident energy is within a window around a feature of interest, most often a full-energy peak associated with a specific decay of a radionuclide. Each cone represents all possible incident directions for a specific gamma-ray, and the accumulation of multiple cones can reconstruct the 2D projection of the gamma-rays [1].

3D Compton imaging can be achieved by performing static measurements, either by using the parallax provided by the extent of the detectors from a single position or by moving the detector to different locations in the scene. To perform these reconstructions, the position and orientation of the detector at each measurement must be known to properly rotate and translate Compton cones, which can be determined manually for static measurements. It is also possible to accomplish 3D imaging while freely moving the system throughout the scene, but this requires some automatic and real time solution (i.e., SLAM) to know the the position and orientation of the detector during each gamma-ray event.

3D image reconstruction speed and noise reduction can be improved by constraining reconstructions to intersections of Compton cones with surfaces present in the scene. Each occupied voxel in the scene (as determined in Sect. II-B) is treated as a volume with a Gaussian width distribution, calculated as the product of the voxel size and $\sqrt{\pi/2}$ to keep the volume of the spherical Gaussian the same as the cubic voxel. To account for uncertainties in the Compton cone axis and opening angle caused by uncertainties in energy deposition and event position, the Compton cones are also given a width described with a Gaussian distribution. The Compton cone width can be calculated on a cone by cone basis, but in this analysis each cone is given a constant conservative value of 14°. The cone-voxel intersection is performed by computing the overlap of the two Gaussian distributions in 3D.

a) Compton response function generation: 3D reconstructions using iterative methods such as MLEM require a response function which characterizes the signal induced by a source at any direction. For the Compton imaging modality, the cone-voxel intersection described in the previous section serves as the 3D response function for the list-mode MLEM formulation (discussed in Section II-D). There is currently no consideration of occlusion from the coded MURA mask, LiDAR, battery, etc. in the response function for the Compton imaging modality.

b) Compton event cuts: Compton imaging is lower efficiency than proximity mapping and coded aperture imaging due to its restrictive event selection. However, the angular resolution is much higher due to the enhanced directional information provided by Compton kinematics.

The depth sensitivity of Polaris-H improves Compton imaging by reducing the uncertainty in the lever arm (distance between two interaction positions). Events are selected which have a lever arm above 2.1 mm to reduce uncertainty in the determination of the scatter axis and remove events with poor angular resolution [1].

In this analysis we consider only double interaction events. The sequence of the two interactions can be ambiguous at some energies. The interaction with the higher energy deposition is often sequenced first, except in physically impossible sequences (e.g., interaction with higher energy deposition is beyond Compton edge) [20] [21]. It is also possible to use the Klein-Nishina cross section to choose the sequence with the more likely probability [20] [22]. These methods can

result in some cones being mis-sequenced, removing accurate cones which can be used to reconstruct source location. It is also possible to use both scattering sequences and to weight each cone based on the likelihood of the scattering sequence it is generated from [23]. One method is to give a higher weight to the cone generated from the sequence where the first interaction has a higher energy deposition. It is also possible to apply a weight based on the Klein-Nishina and photoelectric effect cross sections of the interactions. In this analysis both scattering sequences are considered and no weighting is applied to the cones.

3) Coded aperture imaging: Coded-aperture imaging relies on the signal modulation imposed by both distance and a coded mask created using an array of open and attenuating elements in front of a position-sensitive detector. This method offers higher angular resolution than proximity methods (which have a completely uniform angular response), though at the cost of reconstruction complexity, limited FOV, sensitivity and proneness to artifacts.

Masks are typically square or hexagonal grids with open and filled elements ("binary masks"). Each open mask element acts as a pinhole, projecting an image of the scene onto a detector behind it. The detected image is therefore a number of overlapping projections of the scene. The primary difficulty posed by this is generating mask designs which most clearly separate the projections, and algorithms which can perform this reconstruction efficiently and without introducing artifacts. Though coded-aperture approaches offer a compact, efficient means of imaging high energy photon sources, they do so at the cost of reconstruction complexity.

For a perfectly efficient detector with pixels (indexed k, l), 2D image formation can be represented by the following equation:

$$D_{kl} = \sum_{ij} S_{ij} A_{i+k,j+l} + B \qquad (3)$$

where A represents the binary mask array, B contains all background terms (including dark current associated with electronic noise, gammas transmitted through the mask etc.), D is the detected pattern on the detector face [24] and S represents the source distribution.

We have reformulated this into a 3D problem by assuming:

- a series of observations denoted by time-interval Δt
- a detector with an orientation of $\vec{v}$ observing a source along the ray defined by $\hat{r}_s$
- an angular detector (2D) response characterized across 4π by the function $\gamma_{kl}(\vec{v}, \hat{r}_s)$ (far-field assumption)
- detector and voxel centers defined by x and x_s
- voxel activity Λ_s,
- background dependent on pixel index k, l and time, t

This gives the following expression for rate in each pixel for each time bin:

$$D_{klt} = \sum_{s=1}^{N_{vox}} \frac{\gamma_{kl}(\vec{v}, \hat{r}_s)\Lambda_s \Delta t}{4\pi \|\vec{x}_s - \vec{x}\|^2} + B_{klt}\Delta t, \qquad (4)$$

where attenuation has been neglected.

a) Coded-aperture response function generation: At very low photon energy, the response function can be generated using analytical methods such as ray tracing. In this investigation, there was an apparent need for Monte-Carlo generated response functions which took into account more detailed physics.

These detailed response functions were generated using a script which uses MCNP5 [25] as the simulation backbone. The script generates MCNP5 inputs using a template file containing the detector geometry, each with a cone-source at a point defined by a user-input list of angles. Notably, the model includes objects such as the LiDAR and battery system. The detector tally from each run is then automatically processed as needed in order to generate the response for that given angle. Due to the complexity involved in generating near-field responses which would require distance as well as angle bins, only far-field responses were generated. While invalid for detector-source separations less than approximately ten times the mask dimension, scaling far-field angular responses using the inverse square relationship allows the problem to remain computationally tractable. One resulting map of the detector sensitivity showing the coding imposed by the mask and massive objects in the detector is shown in Fig. 2.
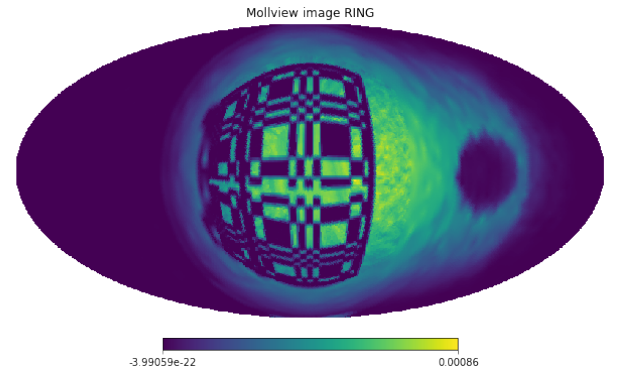

Fig. 2. The sensitivity of a single pixel near the top-center of the the detector volume for a 60keV source plotted across 4π shows the modulation imposed by the mask. The coloring (increasing blue-yellow) denotes sensitivity to a source at that position. The data shown in this Mollweiede plot was the result of several thousand MCNP simulations of point sources at various points across the sphere. The shadow visible at top is due to the LiDAR module, and some slight top/bottom assymetry can be seen due to the attenuation caused by the battery. *Color version of figure is available online.*

b) Coded-aperture event cuts: Events included in the reconstruction are down-selected to remove spurious events which do not contribute to accurate source localization. The primary cut imposed is based on event depth as measured from any detector surface. The concept behind this cut was to remove events in areas of the crystal in which a photoelectric event for a given reconstruction energy would be unlikely. For a given energy window, the attenuation coefficient of CZT is used to calculate an "active depth" in which 99% of incident gamma rays of that energy would be expected to interact. Events beyond this depth from a surface are disregarded, as they are unlikely to be full-energy photoelectric events. However, the crystal dimensions and housing material are not known exactly, so the efficacy of this cut is questionable in

the X-Y plane, and simple Z-depth cuts are used instead.

Events with multiplicity greater than one are discarded (multiple interactions are useful for Compton, rather than coded aperture reconstruction), as are events occurring in "corner" or "edge" pixels on the grid, due to sensitivity variation issues. Additionally, events occurring when Polaris-LAMP is not near a specified area in which reconstruction will be performed are removed (i.e. the analysis can be thought of as a temporal cut consistent with a spectroscopic anomaly or area of interest).

A more advanced cut has also been implemented which uses a combination of event energy, depth and X-Y location to determine the probability of a given event being a full-energy photoelectric absorption or a Compton scattering event which is likely to result from a higher energy photon depositing a portion of its energy. This estimator is designed to provide a background input for a "penalized" list-mode MLEM formulation (discussed in Section II-D), which includes a term to modify the contribution of events based on the probability they are due to background rather than signal (5)).

Given the information available on event location, energy and multiplicity, information on the rate of Compton vs. photoelectric events can be extracted for events in certain energy ranges. For a given photon energy, one can determine a depth in the detector within which nearly all photons of that energy would be expected to interact.

Beyond this defined depth, events of the specified energy are likely to be due to higher-energy photons Compton scattering and depositing a fraction of their energy in the detector. The ratio of these events to events in "allowed" areas of the detector can be used to estimate the background, and be used to create a penalty (term b_n in the list-mode MLEM equation) on a per-timestep basis.

This method for determining background is limited by assumptions about the depth-dependence of spurious event rates and efficiency. For the purposes of this initial investigation, uniform sensitivity is assumed over the first 3 mm.

D. Maximum Likelihood Reconstruction

MLEM is an efficient means of calculating the maximum likelihood estimate of a function from incomplete data. In practice, this algorithm yields high quality reconstructions of 2D and 3D scenes, but at the cost of high computational complexity and propensity to high-spatial-frequency artifacts [26].

This algorithm is used for image reconstruction for all imaging modalities on Polaris-LAMP. The derivation of the MLEM algorithm can be found in [27], [16], [28], while the list mode interpretation [29] is given by

$$\lambda_m^{l+1} = \frac{\lambda_m^l}{\sigma_m} \sum_n \frac{t_{nm}}{\sum_k t_{nk}\lambda_k^l + b_n}, \qquad (5)$$

in which:

- σ_m represents the sensitivity (chance that a given event, indexed by m, is detected at all)
- λ_m^l represents the reconstruction for a given iteration, l

- t_{nm} is the 3D response function sampled on a per-event basis such that it represents the probability that an event emitted in image bin (pixel/voxel) m is detected as event n
- b_n is a background factor for each event

In the case of a detector with a relatively low count rate and a high scene update rate, the list-mode implementation is best used, as each measurement at each pose is starved for counts. In extremely slow moving or extremely high count-rate scenarios, a bin-mode formulation may be appropriate.

III. RESULTS

A. Imaging of Point Sources

A series of measurements were performed to characterize the 3D imaging capability of the proximity mapping, coded aperture, and Compton imaging approaches when locating isolated point sources. These tests consisted of short runs (typically < 60 s) consisting of "natural" paths around a lab space (shown in the top of Figs. 3 and 4) with the detector pointing at the source for only a few seconds of the total run. This was intended to simulate a search scenario in which the source location is not known exactly, but known to be in a room or other confined space. These studies represent a general case in which the nature of the source (point, distributed, etc.) is unknown, which therefore requires the use of the general MLEM reconstruction algorithm.

Online and offline analyses are possible with the Polaris-LAMP system. Online reconstructions can inform the user during the measurement by providing reconstructions and source localization on timescales relevant to the measurement period [1]. The reconstructions in this analysis were produced offline and rendered in a third-party software to generate high quality colorized point clouds. To improve contrast in the images, the colorization in the point cloud is suppressed in the voxels which contain the bottom 10% of reconstruction weight, unless noted otherwise.

A typical example of this test series, shown in Fig. 3, clearly shows that coded aperture imaging provides a significant localization advantage over 3D proximity methods. Using the same dataset and reconstruction parameters (voxelization set at 15 cm, 5 iterations MLEM), proximity reconstruction of the isolated 3.88 MBq (105.1 μCi) ^{133}Ba point source measurement placed significant weight on objects close to the detector path (tables, chairs) as a result of inverse-square sensitivity biasing, and did not identify the source location unambiguously (peak reconstructed intensity was in a voxel over 1 m from the actual source location). The coded aperture reconstruction of the same data (Fig. 3, bottom) identified the source location correctly. The voxel containing the source was assigned a weight 48.7x higher than the mean voxel in the reconstruction, and has the highest weight assigned to any voxel in the model. This finding was robust across a variety of measurements, voxelization schemes and MLEM iteration values.

These runs were also instructive in demonstrating the selectivity of the cuts imposed by the coded aperture reconstruction.

Both proximity and coded aperture reconstructions were performed using a 8 keV wide window on the 81 keV ^{133}Ba peak and the cuts described in the prior section (excluding the background estimator). A total of 844 events out of 32,172 recorded in the run were used for the final reconstruction, reduced based on interaction location (areas deep within the detector are unlikely to have photoelectric events at this energy) and energy-windowing. Though the intent of these tests were not to demonstrate reconstruction in a high-background environment, the measurements nonetheless show the capability to reconstruct from a relatively noisy signal.

A further series of measurements shown in the top of Fig. 4 were conducted with a 7.02 MBq (189.7 μCi) ^{137}Cs source in the same lab environment to characterize the Compton imaging capabilities of Polaris-LAMP. The proximity reconstruction (Fig. 4, middle) with a spectroscopic cut of 662 $\pm$10 keV 29 cm voxels, and 5 iterations of MLEM placed significant weight on other features in the lab, including the shelf above the laboratory bench and other objects on the bench. The image contains two hot spots – one in the voxel where the source is located and another in a voxel containing an adjacent laboratory bench, approximately 64 cm from the source. As noted in Sect. II-C1, artifacts are possible in the proximity modality due to the asymmetry of the system. We believe the incorrect hot spot is a result of the trajectory during the measurement and the naive nature of the proximity mapping method. The two hot spots could correspond to the only points in the cloud equidistant from the detector position where there are significant counts. Further detector motion would then be required to break the degeneracy of the measurement. The incorrect hot spot is given the maximum reconstruction weight, but the voxel containing the source is also assigned a significant weight, 333x that of the mean voxel weight. The Compton reconstruction (Fig. 4, bottom) using the same reconstruction parameters demonstrates the benefit of including direction and energy information. The Compton imaging modality correctly localizes the source intensity to the voxel of the source location, with an assigned weight 4172x greater than mean voxel.

Out of the 20,969 interactions recorded in the run, 3,826 were double interactions, corresponding to 1,913 events eligible for Compton imaging. The lever arm cut removed 206 (11%) of these events. The Compton reconstruction was performed using a 10 keV wide window on the 662 keV ^{137}Cs peak, leaving only 546 Compton cones (double sequenced except when energetically infeasible) for reconstruction. Although the event selection is rather restrictive, the resulting reconstruction demonstrates that it only takes a small fraction of the total events to generate enough Compton cones to locate sources.

B. Imaging of Distributed Sources

A measurement campaign was undertaken at the Paducah Gaseous Diffusion Plant in Kentucky to study the ability of the Polaris-LAMP to characterize a variety of uranium product containers. Several container sizes (e.g., 12B, 30A, 42T) with varying fill materials (including UF$_6$ and UO$_2$) were present.
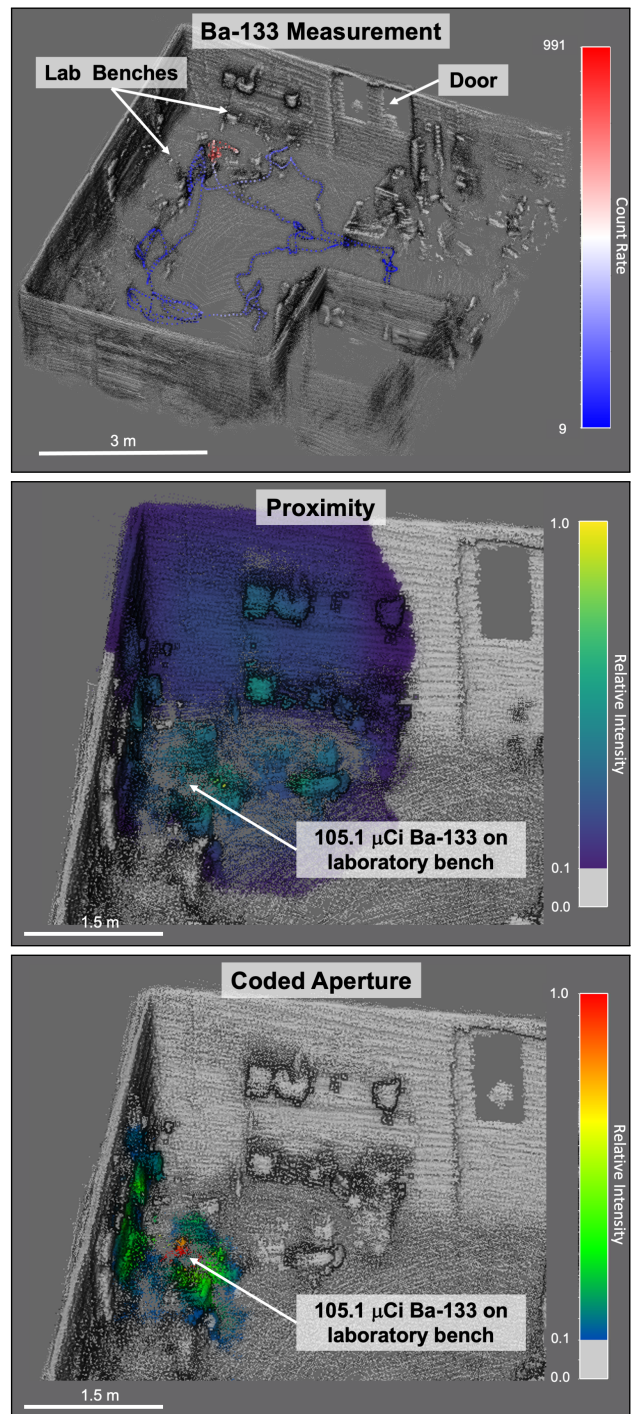

Fig. 3. *Top*: Setup for measurement of 105.1 μCi ^{133}Ba point source placed on a lab bench. Detector path is shown and colorized by gross count rate. *Middle*: Proximity reconstruction using a 77-85 keV window on the 81 keV Ba peak (color scale is relative). Coloration has been suppressed for all voxels with weight <10% max. The signal-to-noise ratio of the Ba peak was 5.52. *Bottom*: Coded aperture reconstruction using the same coloration suppression as the proximity map, 15 cm voxels and 5 iterations of MLEM. This reconstruction correctly identifies the location of the source on the table. *Color version of figure is available online.*

The data were analyzed using the coded-aperture modality to image low-energy (< 300 keV) lines emitted by the tanks, as well as the Compton modality to image the high energy gamma-rays emitted by the daughters of ^{238}U. The proximity
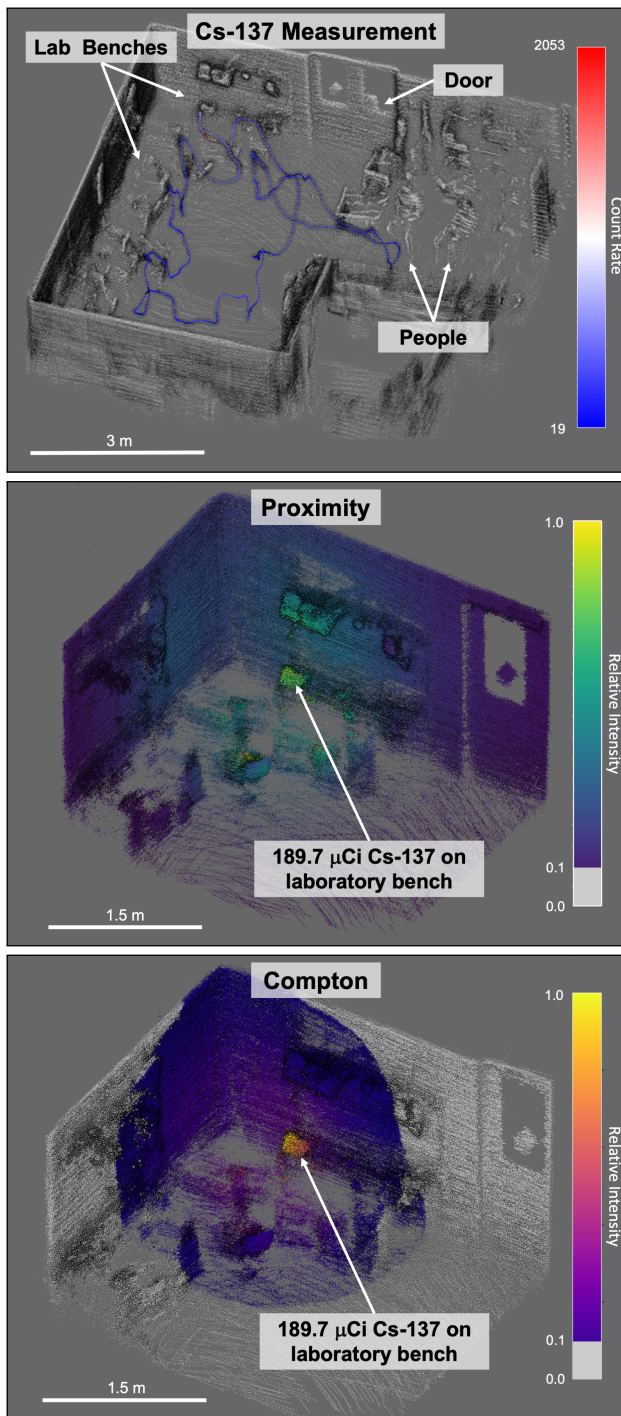
Fig. 4. *Top*: Setup for measurement of a 189.7 μCi ^{137}Cs point source placed on a lab bench in the corner of the room. Detector path is shown and colorized by gross count rate.
Middle: Proximity reconstruction with using a 10 keV window around the 662 keV peak, 7900 occupied voxels with a width of 29 cm, and 5 MLEM iterations. The coloration is suppressed for the bottom 10% of voxels. The signal-to-noise ratio was 12.67 for the Cs peak, with approximately 15 doubles/keV.
Bottom: Compton reconstruction using a 10 keV window around the 662 keV ^{137}Cs peak. The reconstruction consists of 546 cones, 10^6 29 cm voxels, and 5 MLEM iterations. The coloration is suppressed for the bottom 10% of voxels. *Color version of figure is available online.*

mode was omitted from this analysis and focus was placed on the coded aperture and Compton imaging modalities.

The intent of these measurements was to characterize the distribution of material inside the tanks using passive signals. These measurements represent a more challenging reconstruction than that of isolated point sources due to self-attenuation effects and the source spatial extent. The mean free path of 185.7 keV photons (a characteristic ^{235}U line) is on the order of centimeters in solid UF$_6$. The opacity of the tanks causes a large scattering signal, complicating the separation of characteristic lines from background.

A set of dynamic measurements (shown in the top pane of Fig. 5) were performed on three 30A UF$_6$ cylinders located in the tailings yard. Two of these cylinders were effectively empty (those nearest the truck), while the third was loaded to 1/2-2/3 capacity of depleted UF$_6$ (DUF$_6$). Both of the containers had been emptied, but not yet scrubbed with KOH to remove decay products adhered to the walls. Measurements of these tanks were intended to determine if the system could distinguish cylinders containing DUF$_6$ from empty ones, as well as attempt to image the distribution of material in the cylinder. A secondary goal was to determine if notable differences in cleaned and recently emptied tanks were present.

Reconstructions of the three 30A cylinders using the coded-aperture modality were successful in identifying the tank containing DUF$_6$ using the ^{235}U peaks. In the reconstruction shown in Fig. 5 (middle), the mean weight assigned to UF$_6$ tank voxels was approximately a factor of five higher than the emptied and cleaned tank. Reconstructions were also successful using lower energy features (such as U X-rays), though they likewise have poor prominence. Due to the abundance of downscattered photons in the ^{235}U band, some ground-biasing is present (as can be seen in the foreground) and the reconstruction is relatively diffuse. The bottom 10% cut applied to other reconstructions has not been applied to this reconstruction.

A Compton reconstruction was performed on the same dataset using the 1001 keV peak of ^{234m}Pa, the second daughter of ^{238}U. The Compton reconstruction, shown in Fig. 5 (bottom), was also successful in identifying the cylinder furthest from the truck as containing DUF$_6$. Some weight is also given to the cylinders in an adjacent row, as they also contain DUF$_6$, but have thicker walls.

As shown in Fig. 6, the tank yard presents a challenging imaging environment due to the abundance of downscattered photons. Though certain gamma emission lines are visible over the background continuum, imaging these sources is challenging due to the significant scatter component. Improvements to the scatter-to-photopeak event ratio can be made by rejecting events based on interaction location. For a given detected photon energy, events occurring more than two half-value layers from the surface are likely to be Compton scatters rather than valid full-energy deposition photoelectric events.

During the measurements, a spectral feature near 662 keV was identified, as shown in the spectra in Fig. 6. A Compton reconstruction was performed with a 10 keV window on the 662 keV peak using the same dataset as Fig. 5. Fig. 7 shows this reconstruction unambiguously identified the center container as the source of the emission. The energy of the gamma detected and the lack of low-energy features suggests
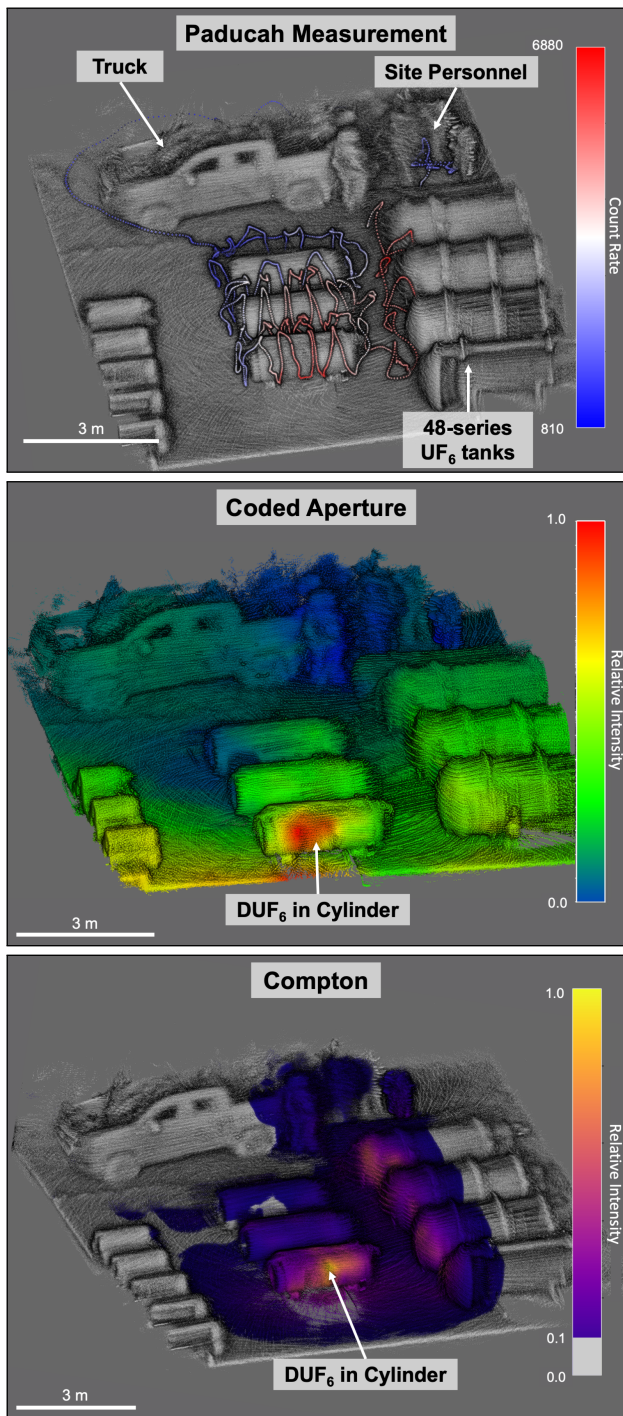
Fig. 5. *Top*: Walking path and count rate during measurement of three 30A cylinders at Paducah.
Middle: Coded-aperture 3D reconstruction performed using 30 cm voxels, 5 iterations of MLEM and a 6 keV window focused on the 185.7 keV line associated with ^{235}U. Signal-to-noise ratio was approximately 1.08 for the peak, with approximately 13k counts/keV.
Bottom: Compton 3D reconstruction performed using 13,000 occupied voxels with a width of 36 cm, 5 iterations of MLEM, and a 10 keV window focused on the 1001 keV peak associated with ^{234m}Pa. The reconstruction consists of 4000 cones. The bottom 10% of voxels are suppressed in this image. The signal-to-noise ratio was 9.49 for the 1001 keV peak, with approximately 100 doubles/keV. *Color version of figure is available online.*

the source is ^{137}Cs, though the origin of this material is unclear as ^{137}Cs is not expected to be found in UF6 tails. The center

cylinder had been recently emptied but not yet cleaned. Prior to this investigation, this anomalous contamination had not been documented.

IV. DISCUSSION

Polaris-LAMP demonstrated significant utility as a proximity mapping, coded-aperture, and Compton imaging system for photons in a variety of environments. The combined modalities provide the ability to localize and map sources across a wide range of energy and source strengths. SDF enables free moving mapping which offers significant sensitivity and localization capability unavailable with traditional methods.

The proximity modality provides limited accuracy and resolution as indicated by the more diffuse activity in the ^{133}Ba and ^{137}Cs point source reconstructions (shown in top of Figs. 3 and 4). The proximity reconstructions showed a bias towards the system as compared to the reconstructions using coded aperture and Compton imaging modalities, as a result of inverse square sensitivity biasing. The maximum voxel weight was assigned at least half a meter from the source location in each reconstruction; however, the voxel where the source was located was also given significant weight.

In coded aperture mode, the detector performs best when imaging or mapping low-energy (< 300 keV) point-like sources, which accords well with the anticipated behavior based on established SNR scaling relations carried over from studies of 2D coded aperture imaging [30]. Polaris-LAMP was shown to operate effectively as a coded aperture imager for both point source and distributed datasets, and shows superior localization as compared with proximity reconstruction. Microcurie-scale point sources in small rooms may be located rapidly (< 60 seconds, depending on scale and activity), while distributed source localization takes longer (on the order of minutes, typically). In a practical exercise, a $10 \mu Ci$ ^{241}Am source placed in an unknown location in a 10×10 m room was isolated in 40 s. While isolated-source performance remains strong, future work will further address the uncertainties of distributed source measurements.

When operating in 3D coded-aperture mode, the localization performance is significantly improved in comparison with proximity-based reconstruction, but is limited by mask fluorescence and near-field effects in addition to LiDAR model problems (SLAM drift, misplaced returns) which apply across all mapping modalities.

In high-background environments, tungsten mask X-ray fluorescence significantly interferes with the ability of the detector to image sources in the 58–61 keV range. Due to the overlap between ^{241}Am characteristic emission lines and W fluorescence, imaging ^{241}Am is difficult in environments with significant high-energy background. Compensating for fluorescence effects is possible, but of limited accuracy due to finite detector resolution that inhibits complete separation of k-α from k-β lines. It is notable that the next generation of coded aperture masks produced by H3D use a thin Cu coating to suppress a significant fraction of the fluorescence [31], though the effectiveness of this method has yet to be examined in depth.
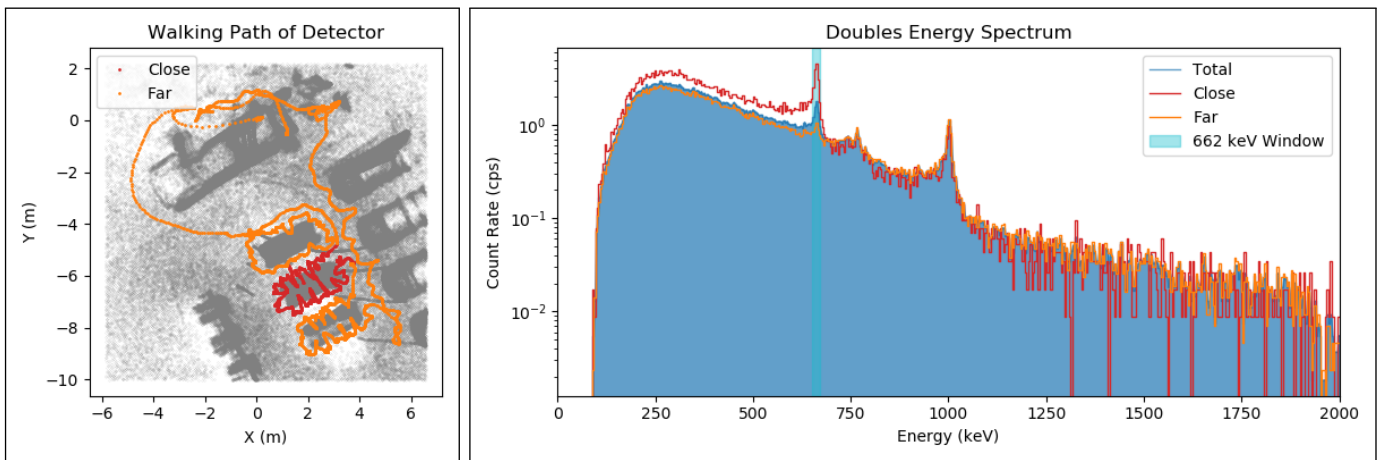
Fig. 6. *Left*: Walking path during Paducah measurement, colorized to show split between portions of measurement deemed 'close' and 'far' from the middle cylinder.
Right: Doubles count rate spectra using 4 keV bins with the 662 +/- 10 keV window highlighted. The 'close' portion of the measurement has a significant 662 keV peak, but further away the peak is reduced. *Color version of figure is available online.*
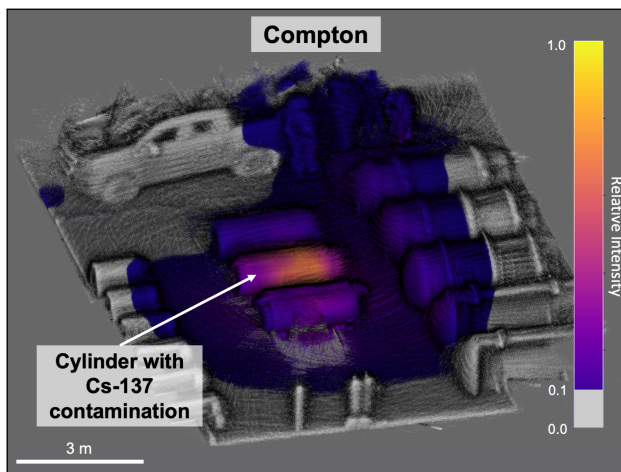

Fig. 7. Compton 3D reconstruction performed with 13,000 occupied voxels with a width of 36 cm, 5 iterations of MLEM and a 10 keV window focused on the 662 keV peak. The reconstruction uses 6500 Compton cones. This reconstruction uses the same data from the measurement shown in Figure 5. The bottom 10% of voxels suppressed in this image. The signal-to-noise ratio was 7.39 for the 662 keV peak, with approximately 200 doubles/keV. *Color version of figure is available online.*

Additionally, "mirroring" artifacts in which multiple instances of the source are shown at regular spatial intervals corresponding to the mask periodicity are evident in some reconstructions. This is an artifact of the tiled-MURA mask design, and may be improved significantly by using a differing mask geometry. Another limitation to the method is driven by the detector's sensitivity to non-coded source. In certain high count rate environments, detector saturation and out-of-FOV sources effects significantly limit the utility of the method [30]. Future work should seek to address these shortcomings through improved mask design and distance-scaled response functions (so called "3D response functions").

Polaris-LAMP was also shown to operate effectively as a Compton imager for both point source and distributed data with photon energies above a few hundred keV (to ensure

a Compton scatter followed by a photoelectric absorption). Although the event selection for Compton imaging is highly restrictive, relatively few events are needed to reconstruct source intensity.

The Compton imaging modality performs well in localizing point sources, assigning a large amount of reconstruction weight to the voxel which contains the source. The 3D free-moving imaging allows reconstruction algorithms to correctly localize source intensity in under one minute. Using 2D reconstruction methods in a "long-dwell, point-and-stare" manner would require much longer measurement times for similar performance. The Compton imaging modality also performs well in distributed source environments, characterizing source environments on the order of minutes.

The Compton imaging modality is constrained by the timing and spatial resolution of the employed detector system. A good timing resolution is required to determine coincident interactions which are used for Compton imaging. Improved timing resolution allows for a smaller coincidence window, allowing for more rejection of background events and enhancing the performance of the system in high background areas. These background events otherwise appear in the data as false coincidences, resulting in false cones being backprojected into the imaging space. As shown in Fig. 5 and Fig. 7, the Polaris detector system performs well in high count rate areas.

The spatial resolution affects Compton imaging results by adding uncertainty to the interaction position which is used to determine the Compton cone axis. There is additional uncertainty in the interaction position associated with the estimated pose from the contextual sensors and SLAM algorithms, which could be improved through the upgrade of these sensors and software. The energy resolution of Polaris adds uncertainty to the scattering angle, which is used as the Compton cone opening angle. These uncertainties in interaction position and energy deposition contribute to the total uncertainty in the backprojected cone, which is accounted for in the Gaussian width distribution of the cones. An improved energy resolution would also allow for narrower energy windows to be set for

reconstructions, further suppressing background events from being included in the Compton analysis.

The lever arm cut which is applied to the data is partially due to the position resolution of Polaris. If the two interactions which comprise a Compton cone are too close to one another, the cone can point in an inaccurate direction which will not be fixed with Gaussian blurring. To avoid this, events with a short lever arm are cut from the reconstruction data. If the position resolution of the detector is improved, the lever arm cut can be smaller, which will increase the number of usable events and the efficiency of the Compton imaging modality.

The accuracy of the system depends on the imaging modality employed. In proximity mode, the peak voxel in the point source reconstructions was at least 0.5 m from the true source location. In the coded aperture and Compton imaging modalities, the reconstruction accurately assigned peak intensity to the voxel containing the source. The resolution of the reconstructions can be measured by the voxel size, which was 15-29 cm in this analysis.

In both Compton and coded aperture modes, LiDAR issues like detector motion artifacts additionally limit the accuracy of reconstructions. High accelerations of the detector system are difficult to accommodate due to the generation of motion trails or diffuse returns in empty space, an artifact of imprecise inputs to the SLAM algorithm. The detector should not be moved or twisted a significant amount between the 10 Hz SLAM refresh rate. For translation movements, this is an insignificant time scale relative to anything that can be walked; however, twisting of the detector (e.g., to survey a cylinder) must be slow and steady. These operational guidelines were followed in the measurements shown. Although Compton and coded aperture modalities have a high angular resolution, inaccuracies in detector location can result in inaccurate reconstructions because the correct pose must be known to backproject in the correct direction.

Though tracks generated by the user's body can be automatically removed from reconstructions, any points missed by the reconstruction algorithm can significantly bias the reconstruction due to their proximity to the detector's path. Sensitivity to a given voxel scales as $\frac{1}{r^2}$, meaning that returns near the detector which are included in the reconstruction accumulate significant weight in reconstruction. Furthermore, portions of the pointcloud that are within the detector's "near field" region (approximately 25 cm for this system) are prone to causing reconstruction distortions, as the far-field coded aperture implementation does not have a means of accurately reconstructing sources in this region.

It is not currently known whether the system is fundamentally limited by the LAMP sensor package or Polaris instrument hardware or software, but this will be analyzed in future work. Future efforts will focus on improving SLAM solution precision and minimizing the latency in pose estimates, as all reconstructions are limited by pose estimation issues.

V. CONCLUSIONS

The Polaris-LAMP platform is the culmination of an effort to fuse SDF capabilities with a COTS semiconductor detector platform. This multimodal system provides a powerful means of performing proximity mapping, coded aperture, and Compton imaging in a variety of environments, and is one of the most compact and versatile detectors with such capabilities. As a proof of concept, we have demonstrated an ability to use it to rapidly map complex environments and to localize anomalous signals while providing rich 3D visualizations. The SDF implementation offers significant benefits to a wide variety of source-search and disaster response tasks, as the high-resolution Compton imaging and coded aperture mask modes provide excellent localization and mapping performance in a robust, portable package.

A notable strength of this system is identifying sources in complex background environments. Due to the use of a COTS CZT detector with high energy resolution ($<1\%$ resolution at 662 keV), the detector offers exceptional ability to reconstruct weak sources in the presence of background, regardless of the imaging modality employed. This capability is shown in the DUF_6 tank surveys where a signal consistent with previously unidentified ^{137}Cs contamination was observed in an empty tank, despite being situated in a large array with several tanks containing DUF_6 (Fig. 7). In this measurement, the count rate in the ^{137}Cs energy window was several orders of magnitude lower than the total count rate. This capability may be of enormous value to accident cleanup, cargo inspections and similar operations in which multiple sources in the same general area must be discerned.

When used as a Compton imager, Polaris-LAMP can be used for imaging both point and distributed source environments, though it excels at the former. The detector performs best when reconstructing energies of at least a few hundred keV to ensure a Compton scatter followed by a photoelectric absorption. However, at high energies the likelihood that there will be a full energy deposition in the detector decreases, which results in loss of Compton cones in the spectroscopic window of interest. High energy background can also result in double interaction events which falsely contribute to the Compton data. The detector performs better when count rates are manageable with the coincidence window, to prevent false coincidences being used to generate Compton cones. Distributed source environments provide a more challenging scenario than point source reconstructions, and should be further analyzed to quantify uncertainties associated with distributed source imaging.

As a coded-aperture imaging system, the detector performs best when measuring low energy sources (less than 300 keV, but ideally less than 150 keV) with well defined emission lines. In the majority of cases in which isolated sources are located in an area with limited contamination, the 3D coded aperture mode provides significant advantages over the proximity mapping modality due to the modulation imposed by the coded-aperture mask. This performance improvement over the proximity case is abundantly evident in the ^{133}Ba localization measurements shown in Fig. 3. These improvements are significant at lower energies, and begin to fade above 200 keV: as the emitter energy trends higher, the coding imposed by the mask is reduced, degrading image quality.

Spatially-extended sources are challenging to reconstruct

due to degraded signal to noise ratios (especially in coded aperture mode) [13]. While extended sources such as UF_6 tanks were reconstructed consistently, with the majority of the weight present in areas where material is known to be present, object boundaries are somewhat blurred due to LiDAR drift and ground scatter. Attempts at characterizing the material distribution within the tanks was not successful, as further work is needed to compensate for self-attenuation using prior knowledge of tank layout. Quantitative investigations of reconstruction performance should be undertaken to discern the ability of the detector to determine the extent of sources within objects using novel voxelization and segmentation schemes.

While the relative color scales used in this document are useful for identifying areas of greater or lesser radioactivity, they are not quantitative measures of emission. Work is ongoing to derive quantitative reconstruction results for coded aperture and Compton imaging modalities.

In summation, the Polaris-LAMP system is a state-of-the-art free-moving gamma-ray imaging system representing the realization of SDF using a high-resolution COTS gamma-ray imager. Full realization of the potential of this concept requires further development. Future work will seek to improve the pose accuracy through upgrade of the contextual sensors and SLAM software, quantitatively characterize the angular response function of the COTS imager, and improve the reconstruction algorithms to enable quantitative gamma-ray imaging while improving reconstruction precision and overfitting. Furthermore, new models of the COTS sensor may incorporate a Cu-coated mask to prevent tungsten fluorescence, while also providing improved performance in high count-rate environments.

VI. ACKNOWLEDGEMENTS

REFERENCES

[1] A. Haefner *et al.*, "Handheld Real-Time Volumetric 3-D Gamma-ray Imaging," *Nucl. Instrum. Methods Phys. Res., Sect. A*, vol. 857, pp. 42–49, 2017.

[2] R. Barnowski *et al.*, "Scene Data Fusion: Real-Time Standoff Volumetric Gamma-ray Imaging," *Nucl. Instrum. Methods Phys. Res., Sect. A*, vol. 800, pp. 65–69, 2015.

[3] A. Zoglauer *et al.*, "First Results of the High Efficiency Multi-Mode Imager (HEMI)," in *Proc. 2009 IEEE NSS/MIC*. IEEE, 2009, pp. 887–891.

[4] J. Jiang *et al.*, "A Prototype of Aerial Radiation Monitoring System Using an Unmanned Helicopter Mounting a GAGG Scintillator Compton Camera," *Journal of Nucl. Sci. Technol.*, vol. 53, no. 7, pp. 1067–1075, Jul. 2016.

[5] S. Joshi *et al.*, "SU-C-201-03: Coded Aperture Gamma-Ray Imaging Using Pixelated Semiconductor Detectors," *Med. Phys.*, vol. 42, no. 6, pt. 3, pp. 3202–3203, 2015.

[6] T. Takahashi *et al.*, "Visualization of Radioactive Substances with a Si/CdTe Compton Camera," in *Proc. 2012 IEEE NSS/MIC*. IEEE, 2012, pp. 4199–4204.

[7] C. G. Wahl *et al.*, "The Polaris-H Imaging Spectrometer," *Nucl. Instrum. Methods Phys. Res., Sect. A*, vol. 784, pp. 377–381, Jun. 2015.

[8] R. Pavlovsky *et al.*, "3-D Radiation Mapping in Real-Time with the Localization and Mapping Platform LAMP from Unmanned Aerial Systems and Man-Portable Configurations," *arXiv:1901.05038*, 2018.

[9] C. G. Wahl *et al.*, "Polaris-H Measurements and Performance," in *Proc. 2014 IEEE NSS/MIC*, 2014, pp. 1–4.

[10] S. E. Anderson *et al.*, "Sub-pixel Position Resolution in Pixelated Semiconductor Detectors," in *Proc. 2007 IEEE NSS*, vol. 2, 2007, pp. 1569–1576.

[11] F. Zhang *et al.*, "Improved Resolution for 3-D Position Sensitive CdZnTe Spectrometers," *IEEE Trans. Nucl. Sci.*, vol. 51, no. 5, pp. 2427–2431, 2004.

[12] S. R. Gottesman and E. E. Fenimore, "New Family of Binary Arrays for Coded Aperture Imaging," *Appl. Opt.*, vol. 28, no. 20, pp. 4344–4352, Oct 1989.

[13] E. Fenimore, "Coded Aperture Imaging: Predicted Performance of Uniformly Redundant Arrays," *Appl. Opt.*, vol. 17, no. 22, pp. 3562–3570, 1978.

[14] W. Hess *et al.*, "Real-Time Loop Closure in 2D LIDAR SLAM," in *Proc. 2016 IEEE Int. Robot. Automat. Conf.*, 2016, pp. 1271–1278.

[15] A. Nüchter *et al.*, "Continuous-Time SLAM—Improving Google's Cartographer 3D Mapping," *Latest Developments in Reality-Based 3D Surveying and Modelling; MDPI: Basel, Switzerland*, pp. 53–73, 2018.

[16] R. Sundberg, "An Iterative Method for Solution of the Likelihood Equations for Incomplete Data from Exponential Families," *Communication in Statistics-Simulation and Computation*, vol. 5, no. 1, pp. 55–64, 1976.

[17] D. Hellfeld *et al.*, "A Spherical Active Coded Aperture for 4π Gamma-Ray Imaging," *IEEE Trans. Nucl. Sci.*, vol. 64, no. 11, pp. 2837–2842, 2017.

[18] D. Hellfeld *et al.*, "Gamma-Ray Point-Source Localization and Sparse Image Reconstruction Using Poisson Likelihood," *IEEE Trans. Nucl. Sci.*, vol. 66, no. 9, pp. 2088–2099, 2019.

[19] J. R. Vavrek *et al.*, "Reconstructing the Position and Intensity of Multiple Gamma-Ray Point Sources with a Sparse Parametric Algorithm," *IEEE Trans. on Nucl. Sci.*, vol. 67, no. 11, pp. 2421–2430, 2020.

[20] D. Xu *et al.*, "4-pi Compton Imaging with Single 3D Position-Sensitive CdZnTe Detector," in *Proc. SPIE 5540, Hard X-Ray and Gamma-Ray Detector Physics VI*, Denver, CO, Oct. 2004, p. 144.

[21] C. Lehner *et al.*, "4-pi Compton Imaging Using a 3-D Position-Sensitive CdZnTe Detector Via Weighted List-Mode Maximum Likelihood," *IEEE Trans. on Nucl. Sci.*, vol. 51, no. 4, pp. 1618–1624, Aug. 2004.

[22] M. Galloway *et al.*, "Simulation and Detector Response for the High Efficiency Multimode Imager," *Nucl. Instrum. Methods Phys. Res., Sect. A*, vol. 652, no. 1, pp. 641–645, Oct. 2011.

[23] A. C. Zoglauer, "First Light for the Next Generation of Compton and Pair Telescopes," Ph.D. dissertation, Max-Planck-Institut für extraterrestrische Physik, 2005.

[24] E. E. Fenimore and T. M. Cannon, "Coded Aperture Imaging with Uniformly Redundant Arrays," *Appl. Opt.*, vol. 17, no. 3, pp. 337–347, 1978.

[25] F. Brown *et al.*, "Mcnp5-1.60 release notes," *Report No. LA-UR-10e06235. Los Alamos, NM: Los Alamos National Laboratory*, 2010.

[26] A. Martineau *et al.*, "Coded Aperture Optimization Using Monte Carlo Simulations," *Nucl. Instrum. Methods Phys. Res., Sect. A*, vol. 616, no. 1, pp. 75–80, 2010.

[27] S. Borman, "The Expectation Maximization Algorithm: a Short Tutorial," 2004. [Online]. Available: http://www.seanborman.com/publications

[28] L. A. Shepp and Y. Vardi, "Maximum Likelihood Reconstruction for Emission Tomography," *IEEE Trans. Med. Imag.*, vol. 1, no. 2, pp. 113–122, 1982.

[29] L. Parra and H. H. Barrett, "List-Mode Likelihood: EM Algorithm and Image Quality Estimation Demonstrated on 2-D PET," *IEEE Trans. Med. Imag.*, vol. 17, no. 2, pp. 228–235, 1998.

[30] R. Accorsi and R. C. Lanza, "Near-Field Artifact Reduction in Planar Coded Aperture Imaging," *Appl. Opt.*, vol. 40, no. 26, pp. 4697–4705, 2001.

[31] C. G. Wahl *et al.*, "Coded-Aperture Imaging with High-Resolution Large-Volume CZT," in *Proc. 2018 IEEE NSS/MIC*. IEEE, 2018, pp. 1–5.